ACS APPLIED OPTICAL MATERIALS

Green Synthesis of Tb^{3+}-Doped $CaMoO_4$ Nanothermometers Using Plant Extract: Enhanced Optical Properties for Temperature Sensing Applications

Daniela F. Duarte, Gilberto J. Arruda, Luiz A. O. Nunes, Sandro M. Lima, and Luis H. C. Andrade*

Cite This: *ACS Appl. Opt. Mater.* 2025, 3, 1810−1820

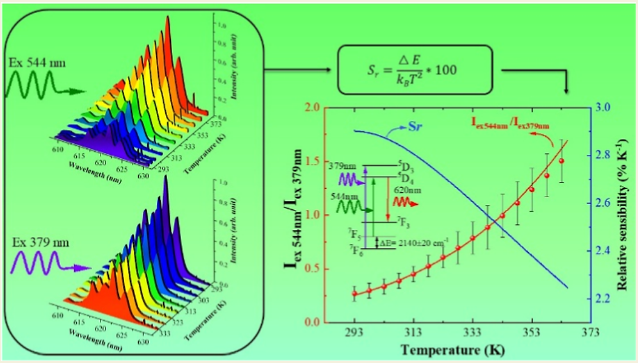

ABSTRACT: Luminescent temperature sensors enable precise thermal monitoring at cellular levels, facilitating cancer treatment approaches and industrial process monitoring across wide temperature ranges. These sensors, when constructed from inorganic matrices incorporating specific luminescence-activating centers, allow temperature estimation through their emission characteristics. This work investigates the optical properties of Tb^{3+}-doped $CaMoO_4$ crystals synthesized via an environmentally friendly coprecipitation method using an extract from the leaves of the *Tabebuia aurea* tree. Spectroscopic characterization confirms the formation of the $CaMoO_4$ crystalline phase and successful incorporation of Tb^{3+} ions into the crystal lattice. Particle morphology was examined using scanning electron microscopy. Temperature-dependent luminescence measurements reveal exceptional performance as an optical sensor, with a calculated relative sensitivity of 2.8% K^{-1} at 363 K, surpassing previously reported values for other Tb^{3+}-doped materials. This green synthesis approach demonstrates that environmentally sustainable methods can produce nanothermometers with enhanced sensing capabilities, surpassing conventionally synthesized alternatives, and with significantly reduced organic residues, which correlates with a superior radiative lifetime and excellent stability and reproducibility for practical applications.

KEYWORDS: *green synthesis, Tb^{3+}-doped calcium molybdate, Tabebuia aurea extract, nanothermometers, luminescence thermometry, environmental sustainability*

1. INTRODUCTION

Temperature measurement is a crucial parameter across numerous technological fields. Conventional methods for temperature monitoring typically employ contact thermometers utilizing thermo-resistive, semiconductor, or thermocouple sensors. However, these devices face significant limitations: they are primarily suited for macroscopic systems, vulnerable to interference from strong electromagnetic fields or radioactivity, and inadequate for monitoring temperature at microscopic or submicroscopic scales.

Thermal imaging cameras represent another widely adopted temperature measurement technique. Their noncontact operation allows simultaneous temperature monitoring across extensive areas, offering considerable versatility. However, accurate calibration requires precise knowledge of the material's local emissivity. Despite advantages over contact methods, thermal cameras exhibit limited spatial resolution, hindering temperature mapping at the microscale or nanoscale.[1]

Significant research has focused on developing luminescent materials for temperature monitoring, leveraging the temperature-dependent luminescence properties of many rare-earth-doped crystals and other luminescent materials.[2] These temperature sensors operate using the fluorescence intensity ratio (FIR) method, which calculates the ratio between emission band intensities at different wavelengths or between emissions at the same wavelength resulting from different excitations.[3,4] The application of nanometer-scale luminescent temperature sensors offers particular promise for monitoring cellular temperature, potentially facilitating cancer treatment. Additionally, these sensors can monitor material temperatures during various thermal processing operations.[5,6]

Calcium molybdate ($CaMoO_4$ or CMO) is an inorganic crystalline structure belonging to the scheelite crystal family. It

Received: June 4, 2025
Revised: August 9, 2025
Accepted: August 11, 2025
Published: August 13, 2025

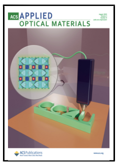

https://doi.org/10.1021/acsaom.5c00208

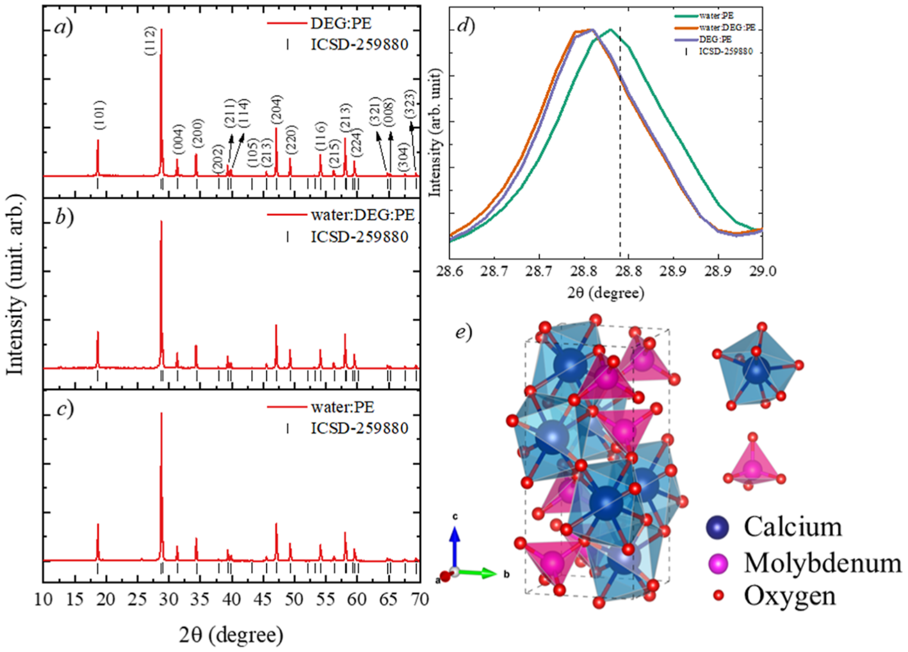

Figure 1. Shows the observed X-ray diffraction of the synthesized samples. (a) water/PE sample and Bragg positions and crystal planes apply to all samples; (b) water/DEG/PE sample; (c) DEG/PE sample. (d) shows the change in peak position compared to the ICSD-259880 standard and (e) illustrates the tetragonal unit cell of $CaMoO_4$ and the CaO_8 and MoO_4 bonds.

Table 1. Lattice Parameters, Unit Cell Volume, Average Crystallite Size, and Percentage of Coincident Crystalline Phase Calculated by Rietveld Refinement for Each Synthesized Tb^{3+}/CMO Sample[a]

samples	identified phases	*a* (Å)	*b* (Å)	*c* (Å)	volume (Å^3)	avg. size (nm)	phases (%)
water/PE	$CaMoO_4$	5.22811 (1.0)	5.22811 (1.0)	11.4376 (0.2)	312.626 (1.1)	51.2 (0.6)	90.93 (18)
	$Mo_4O_{15}Tb_2$	6.686 (1.1)	9.512 (0.6)	10.499 (1.0)	648.6 (1.3)	13.14 (0.5)	9.57 (18)
water/DEG/PE	$CaMoO_4$	5.22887 (0.8)	5.22887 (0.8)	11.43614 (1.7)	312.677 (0.8)	54.9 (1.6)	95.1 (15)
	$TbO_{1.81}$	5.3266 (0.5)	5.3266 (0.5)	5.3266 (0.5)	151.13 (0.3)	57.0 (3.1)	0.91 (10)
	$Tb_2(MoO_4)_3$	9.984 (0.5)	10.592 (0.5)	10.470 (0.5)	1107.3 (0.9)	19.8 (1.2)	1.9 (4)
	terbium oxide	10.77 (0.2)	10.77 (0.2)	10.77 (0.2)	1249 (0.4)	151.6 (77.84)	2.1 (3)
DEG/PE	$CaMoO_4$	5.22835 (0.8)	5.22835 (0.8)	11.43437 (1.8)	312.566 (0.8)	55.2 (1.8)	97.9 (3)
	terbium oxide	9.65 (0.5)	9.65 (0.5)	9.65 (0.5)	899 (0.8)	4.17 (0.8)	2.1 (3)

[a] Values in parentheses are the calculation error.

crystallizes in the $I4_1/a$ (88) space group, featuring Ca–O_8 and Mo–O_4 groupings that share oxygen atoms to form its characteristic crystalline lattice.[7,8] CMO exhibits exceptional thermal and chemical stability, low toxicity, and serves as an excellent host matrix for rare-earth (RE) elements due to its high solubility for most RE elements.[9,10] Additionally, CMO provides a broad transparency range for excitation and emission, spanning from 210 to 750 nm.[11,12]

The terbium ion (Tb^{3+}) is a luminescent species that produces important emission bands across the visible region. Notably, it exhibits a strong emission band near 544 nm, corresponding to the $^5D_4 \rightarrow {}^7F_5$ transition. This ion has been extensively investigated for potential applications in electronic devices, lighting, forensic science, and thermal sensing.[13,14] Tb^{3+}-doped CMO (Tb^{3+}/CMO) can be synthesized through various routes, including solid–state reactions, hydrothermal methods, and coprecipitation techniques.[11,15,16] Synthesis parameters such as temperature, pressure, and reaction media can significantly influence the material's morphology and crystalline structure.[17]

Conventional coprecipitation syntheses typically employ chemical reagents rich in hydroxyl groups to precipitate and stabilize nanoparticles in aqueous solutions. Plant extracts (PE), which contain abundant OH-bonds in their molecular structures, can function similarly in nanoparticle synthesis, achieving effects comparable to those obtained through conventional chemical methods.[18] Beyond simplifying the synthesis process, PE utilization reduces environmental impact from chemical agent disposal and lowers overall synthesis costs.

This study aims to develop an environmentally friendly synthesis route for terbium-doped calcium molybdate (Tb^{3+}/CMO) using PE as a reaction medium. We evaluate the structural, morphological, and luminescent properties of the resulting material for potential temperature sensing applications, with particular focus on achieving enhanced optical performance while reducing environmental impact compared to conventional synthesis methods.

2. RESULTS AND DISCUSSION

2.1. X-ray Diffraction

X-ray diffraction (XRD) analysis was performed on the Tb^{3+}/CMO samples to characterize their crystalline structure. Figure 1 presents the XRD patterns of samples synthesized via three

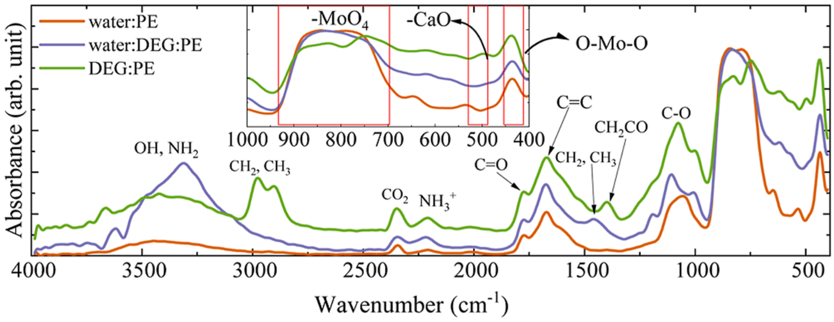

Figure 2. FTIR-PAS spectra of the three synthesized Tb^{3+}/CMO samples. The inset highlights the region from 1000 cm^{-1} to 400 cm^{-1} where metal−oxygen vibrational modes are observed.

distinct routes: (a) water/PE, (b) water/DEG/PE, and (c) DEG/PE. All three diffraction patterns exhibit remarkably similar features, with crystallographic peak positions in excellent agreement with the reference pattern from the ICSD-259880 standard for calcium molybdate. Figure 1d compares the most intense diffraction peak, corresponding to the (112) crystallographic plane. Figure 1e illustrates the structural arrangement of the CaO_8 polyhedra and MoO_4 tetrahedra within the tetragonal unit cell of $CaMoO_4$, highlighting the characteristic bonding configuration of this crystalline material.

Table 1 summarizes the crystallographic parameters obtained from Rietveld refinement analysis for each synthesized Tb^{3+}/CMO sample, including identified crystalline phases, lattice parameters, unit cell volume, average crystallite sizes, and phase percentages. For reference, the ICSD-259880 standard for pure $CaMoO_4$ exhibits lattice parameters of $a = b = 5.22028$ Å and $c = 11.42849$ Å, corresponding to a unit cell volume of 311.710 Å^3. Comparative analysis between the theoretical reference values and our experimentally determined parameters confirms that all synthesized Tb^{3+}/CMO powders crystallize in the tetragonal system with space group $I4_1/a$, consistent with the expected crystal structure of calcium molybdate.

The Rietveld refinement results reveal subtle structural modifications associated with the incorporation of Tb^{3+} dopant ions. The difference in ionic radii between the host Ca^{2+} (1.12 Å) and the dopant Tb^{3+} (1.04 Å) ions in 8-fold coordination sites induces slight shifts in diffraction peak positions toward smaller 2θ angles.[10,14] This observation provides strong evidence that Tb^{3+} ions have successfully substituted into the Ca^{2+} crystallographic sites within the $CaMoO_4$ crystal lattice, resulting in minor but detectable alterations to the unit cell dimensions while maintaining the overall tetragonal structure.

Rietveld refinement analysis confirmed that $CaMoO_4$ constitutes the predominant crystalline phase in all synthesized samples, accounting for more than 90% of the diffraction pattern intensity. Although minor secondary phases were detected across all synthesis routes, the water/PE method yielded the highest phase purity, notably without the formation of cubic terbium oxide as a secondary phase. Structural imperfections within the crystal lattice can originate from several sources, including trace impurities in the precursor materials and lattice distortions induced by the incorporation of Tb^{3+} ions with their different ionic radius and charge compared to Ca^{2+}.[19,20] Furthermore, specific physicochemical conditions during the synthesis process—such as temperature, pH, and reaction kinetics—may influence the formation and distribution of these crystallographic defects.[20] Nevertheless, the minimal presence of secondary phases did not introduce significant structural perturbations that would alter the characteristic 2θ peak positions or substantially modify the overall XRD profile, as evidenced in Figure 1, indicating the robust formation of the desired Tb^{3+}/CMO crystalline structure across all synthesis conditions.

2.2. Middle Infrared Absorption

Figure 2 presents the infrared absorbance spectra for the three synthesized Tb^{3+}/CMO samples. A broad absorption band centered at approximately 3350 cm^{-1} is attributed to O−H stretching vibrations, originating from residual water molecules and hydroxyl groups derived from both the PE and DEG components.[21,22] In the water/DEG/PE sample, distinctive C−H stretching vibration bands at 2974 cm^{-1} and 2899 cm^{-1} clearly confirm the presence of DEG in the final product.[23] Due to the complex biochemical composition of the PE, comprehensive identification of all absorption bands presents a significant challenge. However, based on the known constituents of the extract, several characteristic functional groups can be identified, including CO_2 and C≡N (2347 cm^{-1} and 2218 cm^{-1}), C═O and C═CH (1672 cm^{-1}),[24,25] and various C−O and C−N bonds (in the range of 1500 cm^{-1} to 1000 cm^{-1}).[21]

The inset of Figure 2 highlights the spectral region between 1000 cm^{-1} and 400 cm^{-1}, where the characteristic vibrational modes of the $CaMoO_4$ crystal lattice are prominently displayed. The MoO_4^{2-} tetrahedral group exhibits both symmetric and asymmetric stretching vibrations in the range of 900 cm^{-1} to 700 cm^{-1}, with an additional symmetric stretching mode (O−Mo−O) observed at approximately 400 cm^{-1}.[23,26] Absorption bands associated with Ca−O vibrational modes are evident in the region between 580 cm^{-1} and 500 cm^{-1}.[27,28]

Notably, the water/PE sample demonstrates significantly lower absorption intensity in regions corresponding to −OH, −CH, and CH_3CO functional groups compared to the water/DEG/PE and DEG/PE samples. This observation suggests a reduced concentration of residual organic compounds in the water/PE sample, attributable primarily to the absence of DEG in the synthesis medium. The presence of these organic functional groups, which are likely adsorbed on the particle surfaces, can potentially compromise luminescence intensity by increasing phonon energy in the material, thereby facilitating nonradiative decay pathways that compete with the desired radiative transitions.[29−31] The persistence of these absorption bands even after high-temperature heat treatment at 1173 K indicates that some organic compounds remain strongly bound

https://doi.org/10.1021/acsaom.5c00208
ACS Appl. Opt. Mater. 2025, 3, 1810−1820

to the Tb^{3+}/CMO particles, potentially influencing their optical properties.

2.3. FEG-SEM Microscopy

Figure 3 presents a scanning electron microscopy (SEM) image of the DEG/PE sample, accompanied by elemental composition data obtained through energy-dispersive X-ray spectroscopy (EDX). The weight concentration values, and corresponding mole percentages of the constituent elements are displayed in the upper-left corner of the image. The micrograph reveals a hierarchical morphology characterized by two distinct clusters populations: smaller clusters (highlighted by red circles) with an average diameter of 0.58 μm exhibiting varied morphologies, and larger spherical structures with an average diameter of 3.97 μm that dominate the sample. It is crucial to note that, although SEM reveals these larger structures and aggregates, the nanomaterial classification is based on the dimensions of the primary crystallites, which were determined by X-ray diffraction (XRD) analysis to be 51−55 nm (Table 1). The structures observed by SEM therefore represent aggregates of these nanocrystallites, a common phenomenon in nanomaterials, especially after thermal treatment.

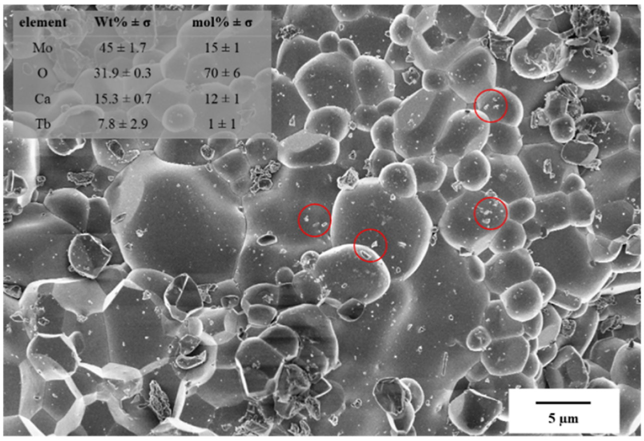

element	Wt% ± σ	mol% ± σ
Mo	45 ± 1.7	15 ± 1
O	31.9 ± 0.3	70 ± 6
Ca	15.3 ± 0.7	12 ± 1
Tb	7.8 ± 2.9	1 ± 1

Figure 3. SEM image of the DEG/PE sample. The table in the upper left corner presents the EDX results as a weight percentage for the elements Mo, Ca, O, and Tb. The red circles highlight the smallest structures formed.

The observed morphological characteristics can be attributed to the interplay of several synthesis parameters, particularly the solubility behavior of the salt precursors in the reaction medium and the degree of supersaturation achieved during precipitation. Previous studies have established that synthesis temperatures below 373 K typically promote the formation of larger particles, which aligns with our observations given that the synthesis was conducted at 363 K followed by thermal treatment at 1173 K which promotes sintering and agglomeration processes.[14,32,33]

2.4. Spectroscopic Characterization

Figure 4a presents the normalized excitation and emission spectra of Tb^{3+}/CMO samples synthesized via three different routes, alongside an undoped CMO reference sample. The excitation spectra exhibit a characteristic broad band extending from 220 to 350 nm across all samples. In the case of the undoped CMO reference, a broad emission band spanning from 400 to 750 nm is observed, originating from intrinsic transitions within the MoO_4^{2-} tetrahedral groups.[34,35] For clarity of comparison, this spectrum has been normalized in intensity; it is important to note that the original emission intensity of undoped CMO was significantly lower than that of the Tb^{3+}-doped samples.

The emission spectra of all Tb^{3+}-doped samples display well-defined, sharp emission lines centered at 488, 544, 586, and 620 nm, which are attributed to the $^5D_4 \rightarrow {}^7F_6$, $^5D_4 \rightarrow {}^7F_5$, $^5D_4 \rightarrow {}^7F_4$, and $^5D_4 \rightarrow {}^7F_3$ electronic transitions within the Tb^{3+} ion, respectively.[36] The precise wavelength positions of these emission bands remain consistent across all three synthesis routes, resulting in the superposition of the normalized emission spectra for the differently synthesized Tb^{3+}/CMO samples.

Figure 4b illustrates the proposed energy transfer mechanism responsible for the enhanced luminescence in the Tb^{3+}/CMO materials. Following photoexcitation, the MoO_4^{2-} ions absorb incident energy and subsequently transfer this excitation energy to neighboring Tb^{3+} ions, promoting them

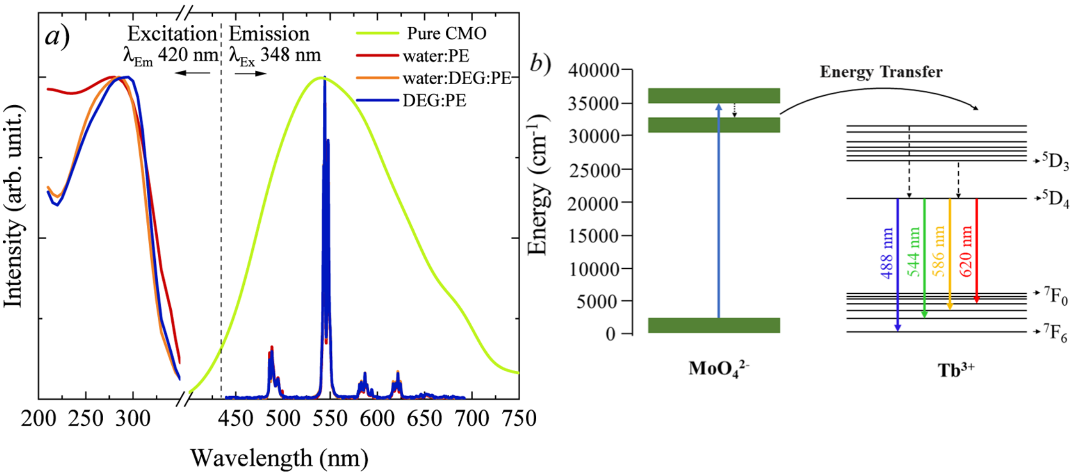

Figure 4. (a) Excitation and emission spectra of the Tb^{3+}/CMO and undoped CMO sample. Note that the pure CMO emission was normalized in intensity for visual comparison with the Tb^{3+}/CMO emissions, with its original intensity being significantly lower than that observed for the Tb^{3+}-doped samples. (b) Schematic illustration of the energy transfer mechanism from MoO_4^{2-} to Tb^{3+} ions, including nonradiative decay (dotted arrow) to the $^5D_4$ level and subsequent radiative emission.

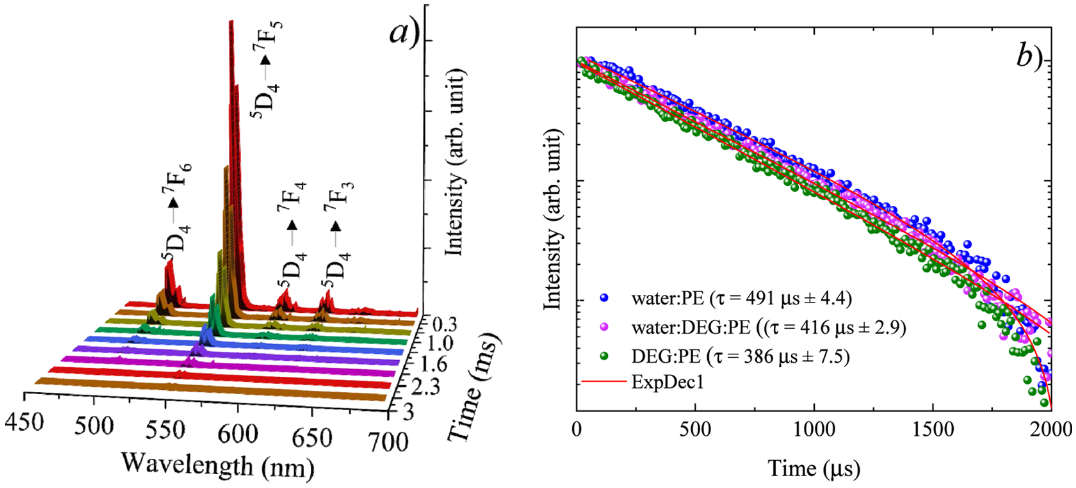

Figure 5. (a) Time-resolved luminescence spectra of the Tb^{3+}/CMO water/PE sample under 358 nm excitation. (b) Luminescence decay curves at 544 nm for the water/PE, water/DEG/PE, and DEG/PE samples under 358 nm excitation.

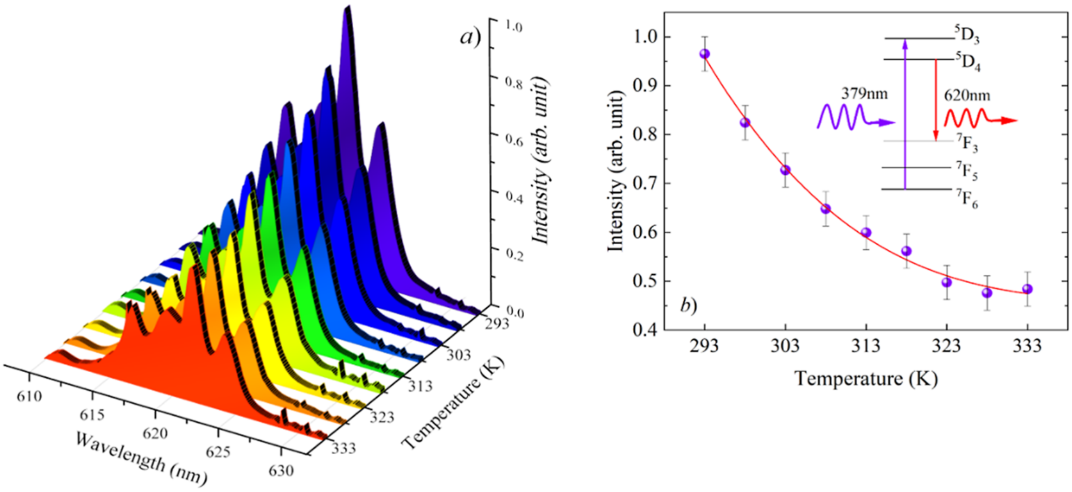

Figure 6. Temperature-dependent luminescence of the Tb^{3+}/CMO water/PE sample under 379 nm excitation. (a) Temperature-dependent luminescence intensity. (b) Integrated luminescence intensity as a function of temperature.

to higher energy states. The excited Tb^{3+} ions then undergo initial nonradiative relaxation to the $^5D_4$ metastable level, followed by radiative transitions to the various ^7F_J (J = 6, 5, 4, 3) terminal states. This energy transfer process significantly enhances the luminescence efficiency of the material compared to direct excitation of the Tb^{3+} ions, resulting in the characteristic emission spectrum dominated by the strong green emission at 544 nm ($^5D_4 \rightarrow {}^7F_5$ transition).[34,37]

Figure 5a presents the time-resolved luminescence spectrum of the Tb^{3+}/CMO water/PE sample under excitation at 358 nm. The spectrum exhibits well-resolved emission lines of the Tb^{3+} ion.[37] This characteristic emission profile is consistently observed across all three Tb^{3+}/CMO samples synthesized via different routes, confirming the successful incorporation and optical activation of Tb^{3+} ions in each case. Figure 5b illustrates the luminescence decay profiles for the prominent 544 nm emission ($^5D_4 \rightarrow {}^7F_5$ transition) under 358 nm excitation for all three samples: water/PE, water/DEG/PE, and DEG/PE. The decay kinetics in each case are accurately modeled by a single exponential function,[30] indicating a homogeneous distribution of Tb^{3+} ions within the $CaMoO_4$ crystal lattice and the absence of significant energy transfer between neighboring Tb^{3+} ions at the 5% doping concentration. The calculated radiative lifetimes (τ) for the water/PE, water/DEG/PE, and DEG/PE samples are 491, 416, and 386 μs, respectively. These values align well with previously reported lifetimes for Tb^{3+}-doped materials in the literature.[38−40] Notably, the water/PE sample exhibits a significantly longer decay time compared to the other synthesis routes, suggesting a reduced probability of nonradiative relaxation from the $^5D_4$ excited state via phonon-assisted processes. This observation correlates directly with the FTIR-PAS results presented in Figure 2, which demonstrated lower absorption intensity in the 2000−4000 cm^{-1} region for the water/PE sample. The reduced presence of high-energy vibrational modes (such as O−H, C−H, and other organic functional groups) in this sample minimizes nonradiative quenching mechanisms, thereby enhancing the radiative lifetime and potentially improving the overall luminescence efficiency of the material.

2.5. Luminescence Temperature Sensors

The potential application of Tb^{3+}/CMO as an optical temperature sensor was evaluated using the water/PE synthesized sample, which was selected based on several advantageous characteristics: its straightforward synthesis

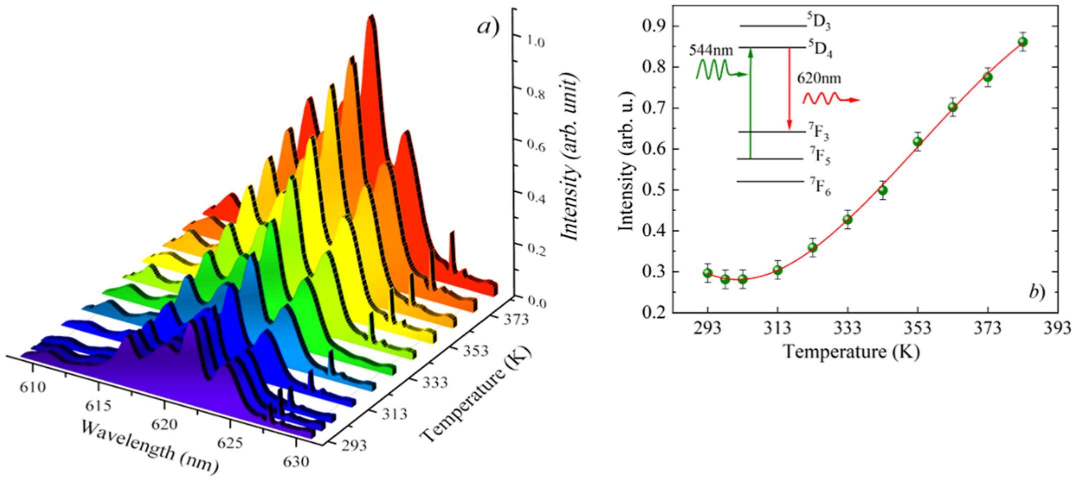

Figure 7. Temperature-dependent luminescence of the Tb^{3+}/CMO water/PE sample under 544 nm excitation. (a) Temperature-dependent luminescence intensity. (b) Integrated luminescence intensity as a function of temperature.

protocol, minimal presence of luminescence-quenching molecular groups (as evidenced by FTIR-PAS analysis), and superior radiative lifetime performance. Figure 6a presents the temperature-dependent luminescence spectra under 379 nm excitation, with measurements conducted across a temperature range from 293 to 333 K. A systematic decrease in luminescence intensity is observed with increasing temperature across the entire emission spectrum, particularly for the dominant $^5D_4 \rightarrow {}^7F_3$ transition.

Figure 6b illustrates the integrated luminescence intensity as a function of temperature, showing a clear inverse relationship. The observed thermal quenching behavior can be explained through the underlying energy level dynamics: upon 379 nm excitation, electrons are promoted from the $^7F_6$ ground state to the $^5D_3$ excited state, followed by rapid nonradiative relaxation to the metastable $^5D_4$ level, and subsequent radiative transition to the $^7F_3$ terminal state. As temperature increases, thermal energy facilitates the population of higher energy thermally coupled levels, such as the $^7F_5$ state, effectively reducing the population available in the $^7F_6$ ground state for excitation.[41] This temperature-induced redistribution of electronic populations results in the observed systematic decrease in emission intensity, providing a reliable basis for temperature sensing applications through calibrated intensity measurements.

Figure 7a displays the temperature-dependent luminescence spectra under 544 nm excitation, with measurements conducted across an extended temperature range from 293 to 383 K. In striking contrast to the behavior observed under 379 nm excitation, the emission intensity exhibits a systematic increase with rising temperature across all emission bands. Figure 7b quantifies this relationship by plotting the integrated luminescence intensity as a function of temperature, revealing a clear positive correlation. This distinctive thermal behavior can be attributed to the unique excitation pathway involved: 544 nm excitation selectively promotes electrons from the thermally populated $^7F_5$ level directly to the $^5D_4$ excited state. At lower temperatures, the electron population predominantly occupies the $^7F_6$ ground state, with minimal thermal population in the higher energy $^7F_5$ level. However, as temperature increases, thermal energy facilitates the population transfer from the $^7F_6$ ground state to the $^7F_5$ level through thermal coupling between these states, thereby increasing the available population for the $^7F_5 \rightarrow {}^5D_4$ absorption process.

This temperature-dependent population redistribution follows Boltzmann's distribution law, which predicts an exponential increase in the population of higher energy states with increasing temperature.[42,43] Consequently, the enhanced thermal population of the $^7F_5$ level results in more efficient absorption of the 544 nm excitation, leading to the observed enhancement of emission intensity with increasing temperature. This phenomenon provides an alternative temperature sensing mechanism with enhanced sensitivity at elevated temperatures, complementing the conventional thermal quenching approach.

In contrast to conventional FIR approaches that utilize a single excitation to monitor the ratio of two distinct emissions, this work employs an advanced strategy based on the excitation of thermally populated levels. This dual-excitation methodology, which monitors a single emission line (620 nm) under different excitation wavelengths (379 and 544 nm), offers significant advantages, such as simplifying the detection system and the ability to achieve superior sensitivities, as demonstrated by recent studies in the field of optical thermometry.[44,45] The fluorescence intensity ratio (FIR) method was employed to determine the thermal parameter (R) by calculating the ratio between the integrated intensities (I) of the $^5D_4 \rightarrow {}^7F_3$ transition (620 nm) under two different excitation wavelengths, from the $^7F_5$ to $^5D_4$ level (λ_{ex} = 544 nm) and from the $^7F_6$ to $^5D_4$ level (λ_{ex} = 379 nm)

$$R = \frac{I_{\lambda_{ex}=544\,\mathrm{nm}}}{I_{\lambda_{ex}=379\,\mathrm{nm}}} = Be^{-\Delta E/k_B T} \tag{1}$$

in which ΔE represents the energy difference between the $^7F_5$ and $^7F_6$ levels, k_B is the Boltzmann constant, and T is the temperature. The temperature relative sensitivity (S_r) can be calculated theoretically using the following equation

$$S_r = \frac{1}{R}\left|\frac{\mathrm{d}R}{\mathrm{d}T}\right| = \frac{\Delta E}{k_B T^2} \times 100\% \tag{2}$$

Figure 8 shows the luminescence intensity ratio (R) as a function of temperature, along with the calculated relative thermal sensitivity. The inset energy level diagram illustrates the excitation wavelengths (379 and 544 nm) used to excite the $^7F_6$ and $^7F_5$ levels, respectively, and the monitored emission at 620 nm. The energy difference (ΔE) between the $^7F_5$ and

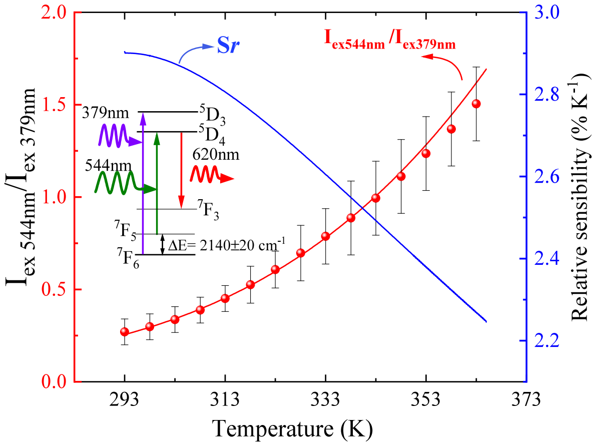

Figure 8. Ratio of intensity (red line) as a function of temperature and relative sensitivity (blue line) to intensity ratio.

$^7F_6$ levels, determined by fitting the intensity ratio R using eq 1, was found to be 2140 cm^{-1}, which is in good agreement with the expected energy difference for Tb^{3+} ions.[46] The calculated maximum relative sensitivity (S_r) was 2.8% K^{-1} at 363 K.

Table 2 presents a comparison between the relative sensitivity obtained in this work and those reported for different Tb^{3+}-doped matrices. The relative sensitivity of the sample synthesized by the water/PE route demonstrates excellent potential for temperature sensing applications using the FIR method, surpassing the values reported in the literature.

Table 2. Comparison between the Relative Thermal Sensitivities Found in Different Works

materials	range of temperature (K)	maximum S_r (% K^{-1})	reference
Tb^{3+}/CMO	293−383	2.8	this work
YPO_4/Tb^{3+}, Ho^{3+}	310−550	2.6	46
$Tb^{3+}/Pr^{3+}/NaGd(MoO_4)_2$	303−483	2.05	58
β-$NaYF_4/Ce^{3+}/Tb^{3+}/Eu^{3+}$	303−563	1.17	59
Ce^{3+}, Tb^{3+}/LaOBr	293−473	1.40	60
$Tb^{3+}/CsPbI_3$	80−480	1.78	61

2.6. Particle Size and Morphology Effects on Temperature Sensing Performance

The exceptional thermal sensitivity achieved in this work (2.8% K^{-1} at 363 K) can be attributed to optimized particle size and morphological characteristics that fundamentally govern the physical mechanisms underlying temperature sensing performance. The relationship between synthesis conditions and particle morphology exerts significant influence on the material's optical properties and thermometric capabilities through several interconnected physical phenomena operating across multiple length scales.[47]

According to Table 1, our $CaMoO_4/Tb^{3+}$ systems show crystallite sizes of 51−55 nm, this scaling critically affects both luminescence intensity and thermal sensitivity through multiple pathways, where surface Tb^{3+} ions experience different local environments compared to bulk ions, with modified coordination numbers and altered crystal field symmetries that enhance the thermal population redistribution between $^7F_5$ and $^7F_6$ levels.[48]

Quantum confinement and energy transfer mechanisms assume increasing importance as particle dimensions approach nanoscale regimes. The primary energy transfer pathway, involving charge transfer from MoO_4^{2-} host groups to Tb^{3+} activator ions, becomes optimized at the observed crystallite dimensions to maximize the fluorescence intensity ratio response to temperature variations. In reduced crystallite dimensions, the average separation distance between MoO_4^{2-} and Tb^{3+} ions decreases, thereby enhancing energy transfer efficiency according to established dipole−dipole interaction mechanisms while maintaining sufficient thermal coupling between the $^7F_5$ and $^7F_6$ thermally coupled levels.[49]

Phonon interactions and thermal coupling undergo fundamental modifications in nanostructured materials. Surface phonon modes contribute increasingly to the phonon density of states as particle size decreases, resulting in altered electron−phonon coupling strengths and modified multiphonon relaxation rates that directly enhance the temperature-dependent population redistribution mechanisms underlying thermometric response.[50] The observed maximum relative sensitivity of 2.8% K^{-1} at 363 K represents an optimization of these size-dependent effects, whereby the 51−55 nm crystallite dimensions provide sufficient quantum confinement benefits and enhanced thermal coupling while avoiding excessive surface quenching phenomena that would compromise fluorescence intensity ratio measurements.[50]

Morphological hierarchy considerations are also critical for practical thermometric applications, as our materials exhibit a hierarchical structure where nanoscale crystallites (51−55 nm) aggregate into larger microscale particles (0.58−3.97 μm), providing advantages for temperature sensing: the nanoscale crystallites maintain enhanced thermal responsiveness through quantum size effects and optimized phonon coupling, while the larger agglomerates offer improved handling characteristics and thermal equilibration properties essential for accurate temperature measurements.[51]

The water/PE synthesis route produces materials with optimal crystallite dimensions that balance quantum confinement benefits with practical luminescence efficiency and thermal sensitivity, where controlled synthesis conditions enable tuning of the sensitivity versus stability trade-offs essential for high-performance thermometric applications. These fundamental relationships between particle characteristics and thermal sensing performance demonstrate how morphological control through green synthesis strategies can achieve superior thermometric capabilities compared to conventional synthesis methods.

2.7. Advantages of Green Synthesis Approach

The plant extract-mediated synthesis employed in this work offers significant advantages over conventional methods for producing Tb^{3+}-doped $CaMoO_4$ nanothermometers. While thermal treatment at 1173 K remains necessary for optimal crystallinity, the key benefits manifest during the synthesis stage and in the final material properties.

Our coprecipitation occurs at mild conditions (363 K) using aqueous *Tabebuia aurea* (Bignoniaceae) extract, contrasting with conventional methods that require high-pressure autoclaves (hydrothermal), multistep procedures with organic solvents (sol−gel), or mechanical grinding with repeated high-temperature treatments (solid-state).[52] The plant extract's phytochemicals serve as both reducing and stabilizing agents, eliminating toxic solvents (ethylene glycol, methanol) and hazardous reducing agents (sodium borohydride, hydrazine) typically required in conventional synthesis.[18,53]

Importantly, FTIR-PAS analysis demonstrates that the water/PE route produces materials with significantly reduced organic residues compared to diethylene glycol-containing samples, even after identical thermal treatment. This cleaner synthesis correlates directly with superior optical properties: longer radiative lifetime (491 μs) and maximum relative sensitivity (2.8% K^{-1}), surpassing previously reported values for Tb^{3+}-doped thermometers. The approach also provides 30−40% reduction in chemical costs through elimination of expensive reagents,[54] while natural capping agents achieve optimal morphological control without synthetic surfactants.[55,56]

These advantages—reduced environmental impact, simplified processing, lower costs, and enhanced optical performance—establish plant-mediated synthesis as a superior route for next-generation luminescent nanothermometers.

2.8. Stability, Reproducibility and Uncertainty for Practical Applications

The fundamental stability of our nanothermometers stems from the robust scheelite crystal structure of $CaMoO_4$, which exhibits exceptional thermal and chemical resistance with a melting point exceeding 1400 °C.[17,40] The successful incorporation of Tb^{3+} ions into the Ca^{2+} crystallographic sites, confirmed by XRD analysis showing minimal lattice distortion, ensures strong ionic bonding that maintains structural integrity across the operational temperature range. The shielded nature of 4f electrons in rare earth ions provides inherent photostability,[44] while the energy transfer mechanism from MoO_4^{2-} groups to Tb^{3+} ions offers additional protection against photodegradation by reducing direct UV exposure to the luminescent centers.[57]

To evaluate the reproducibility and thermal stability of our materials, comprehensive cycling studies were conducted where the error bars in Figure 8 represent measurement uncertainty obtained from five independent thermal cycles. Each sample was systematically heated and cooled across the entire temperature range (293−383 K) to verify the reversibility and reproducibility of the thermometric response. These rigorous tests confirm minimal hysteresis or drift in the fluorescence intensity ratio (544 nm/379 nm excitation), demonstrating exceptional thermal cycling stability essential for long-term deployment.[58] The energy difference (ΔE = 2140 cm^{-1}) between thermally coupled $^7F_5$ and $^7F_6$ levels aligns with established spectroscopic constants for Tb^{3+} ions,[42,45] providing confidence in calibration stability governed by fundamental thermodynamic principles rather than material-specific properties prone to drift.

The uncertainty in thermal sensitivity measurements was comprehensively evaluated considering multiple sources of experimental error. Temperature control using the Lake Shore model 331S controller provides stability within ±0.1 K, while fluorescence intensity measurements show relative uncertainties of ±1.2−2.8% (error bars in Figure 9). Additional uncertainties from spectral resolution (±0.5%) and sample positioning (±1.0%) were incorporated through standard error propagation analysis. The maximum relative sensitivity of 2.8% K^{-1} at 363 K has an associated uncertainty of ±0.2% K^{-1}, corresponding to a minimum detectable temperature change of ±0.4 K and confirming the statistical significance of our measurements well above the noise level.

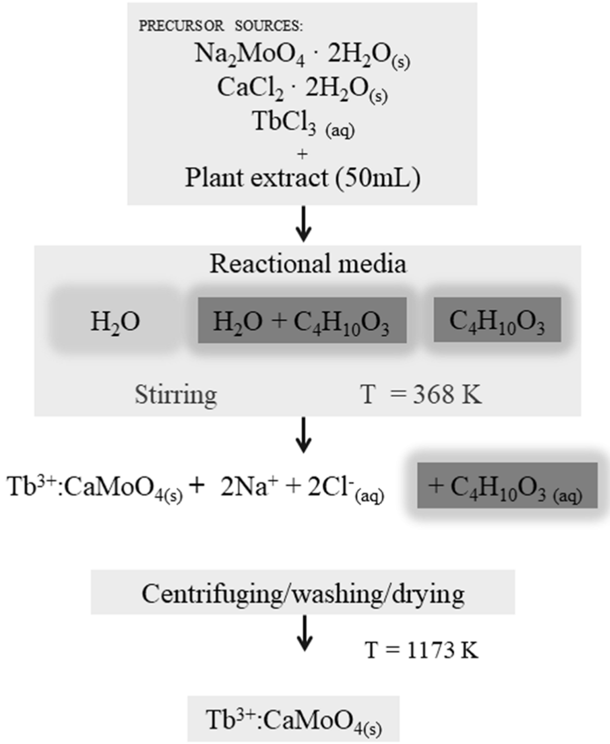

Figure 9. Simplified flowchart of CMO/Tb^{3+} syntheses in different reaction media. Dark gray frames are used to represent syntheses using DEG.

Recent advances in rare earth luminescent materials emphasize the importance of extreme long-term stability for practical applications,[2] and our maximum relative sensitivity of 2.8% K^{-1} significantly surpasses other Tb^{3+}-doped thermometers, providing sufficient sensitivity margins to accommodate any minor long-term variations while maintaining practical utility. The combination of robust host matrix, stable rare-earth luminescence, minimal organic content, demonstrated thermal cycling reproducibility, and agreement with physical constants establishes these environmentally synthesized nanothermometers as promising candidates for reliable, long-term temperature sensing applications across biomedical, industrial, and technological fields.

3. CONCLUSION

This study successfully demonstrates that green synthesis using *T. aurea* plant extract provides a superior route for producing high-performance Tb^{3+}-doped $CaMoO_4$ nanothermometers. The environmentally friendly approach achieved remarkable optical properties, with a maximum relative sensitivity of 2.8% K^{-1} at 363 K—significantly exceeding previously reported values for Tb^{3+}-based thermometers. The water/PE synthesis route yielded materials with optimal characteristics: tetragonal $CaMoO_4$ structure with >90% phase purity, reduced organic residues leading to enhanced radiative lifetime (491 μs), and hierarchical morphology balancing nanoscale properties with practical handling.

Beyond performance advantages, this green synthesis method offers compelling practical benefits: 30−40% reduction in production costs, elimination of toxic solvents and hazardous reducing agents, and simplified single-step processing at mild conditions (363 K). The demonstrated thermal cycling stability and reproducibility, combined with the robust scheelite crystal structure, establish these materials as reliable candidates for long-term temperature sensing applications in biomedical and industrial fields.

This work advances the paradigm shift toward sustainable nanomaterial production, proving that environmental responsibility and superior performance are not mutually exclusive but synergistic goals. Future investigations exploring other plant extract systems and rare-earth dopants could further expand the potential of green synthesis approaches for next-generation luminescent sensors.

4. EXPERIMENTAL METHODS

4.1. Synthesis of Plant Extract (PE)

The PE was prepared from leaves of *T. aurea*. Fresh leaves were collected, thoroughly washed with distilled water, and dehydrated at 343 K (70 °C) until completely dry. To prepare the extract, 10 g of the dried, crushed leaves were combined with 100 mL of distilled water in a suitable vessel. This mixture was heated with continuous stirring at 363 K (90 °C) for 10 min, then removed from heat and allowed to cool to room temperature. The cooled solution was subsequently filtered to remove plant debris, yielding the final PE for use in synthesis.

4.2. Synthesis of Tb^{3+}-Doped CMO

Sodium molybdate dihydrate ($Na_2MoO_4 \cdot 2H_2O$, 99.0%) and calcium chloride dihydrate ($CaCl_2 \cdot 2H_2O$, 99.0%) were employed as sources of molybdate (MoO_4^{2-}) and calcium (Ca^{2+}) ions, respectively, with each reagent used at a concentration of 2.5 mmol. The synthesis reactions were conducted using three different primary solvent systems: (i) distilled water, (ii) a 1:1 volume mixture of distilled water and diethylene glycol ($C_4H_{10}O_3$, DEG), or (iii) DEG alone.

For each synthesis, the reaction medium was prepared by combining 50 mL of the selected primary solvent system with 50 mL of the previously prepared plant extract (PE), yielding a total initial reaction volume of 100 mL. This 100 mL PE-solvent mixture was then heated to 363 K and maintained at this temperature under constant stirring at 1200 rpm. Sequentially, the solid $Na_2MoO_4 \cdot 2H_2O$ precursor was added to the stirred solution, followed by the addition of the solid $CaCl_2 \cdot 2H_2O$ precursor. Doping with Tb^{3+} ions was subsequently accomplished by introducing an aqueous $TbCl_3 \cdot 6H_2O$ (99.9%) solution, calculated to provide Tb^{3+} ions at a 5% molar ratio relative to the $CaMoO_4$ host (equivalent to 125 μmol of Tb^{3+}).

After the addition of all precursors, heating was discontinued, while stirring was maintained for an additional 30 min as the solution gradually cooled to room temperature. The resulting precipitated solid powders were collected via centrifugation at 3100 rpm for 30 min. The isolated powders were then subjected to a purification protocol consisting of four washes with distilled water, followed by two washes with ethanol to eliminate any residual soluble compounds from the reaction. The purified samples were dried at room temperature in Petri dishes, pulverized using an agate mortar and pestle, and then thermally treated at 1173 K (900 °C) for 24 h in a muffle furnace. Following cooling, the heat-treated samples were ground again and prepared for subsequent characterization. For comparative purposes, an undoped $CaMoO_4$ (CMO) sample was also synthesized using the distilled water and PE reaction medium (water/PE route), following the same procedure described above but without the addition of the $TbCl_3$ solution.

Figure 9 presents a flowchart summarizing the reaction processes occurring in the three different synthesis media: water/PE, water/DEG/PE, and DEG/PE. The synthetic pathway involves the addition of precursors to the reaction media, wherein the Ca^{2+} cations and MoO_4^{2-} anions are electrostatically attracted to each other due to their opposite charges, resulting in the precipitation of CMO. The Na^+ and Cl^- counterions, along with any residual organic matter, remain in the supernatant and are subsequently removed during the washing procedure and thermal treatment.

4.3. Structural and Morphological Characterization

X-ray diffraction (XRD) patterns were collected using a Rigaku diffractometer (Mini Flex 600) equipped with a Cu K_α radiation source operating at 40 kV (λ = 0.154 nm). Diffraction data were recorded in the 2θ range from 10° to 70° with a step size of 0.02°. Rietveld refinement analysis was performed using the FullProf Suite software package, employing the International Crystal Structure Database (ICSD) standard 259880 for $CaMoO_4$ powder as a reference. VESTA software was utilized to visualize the $CaMoO_4$ unit cell structure and to identify the corresponding crystallographic planes (*hkl*).

Fourier-transform infrared photoacoustic spectroscopy (FTIR-PAS) measurements were conducted on the $Tb^{3+}/CaMoO_4$ samples using a Thermo Nicolet Nexus 670 spectrophotometer. Spectra were acquired in the wavenumber range from 4000 cm^{-1} to 400 cm^{-1} under a helium gas atmosphere within the photoacoustic cell, with the instrument purged with dry air. Each spectrum represents the accumulation of 128 scans to ensure optimal signal-to-noise ratio.

Morphological examination and elemental composition analysis were performed using field-emission gun scanning electron microscopy (FEG-SEM) coupled with energy dispersive X-ray spectroscopy (EDX).

4.4. Optical Characterization

Excitation spectra were recorded using a PerkinElmer fluorescence spectrophotometer (LS 55) scanning in the wavelength range from 210 to 360 nm. Luminescence measurements, time-resolved luminescence spectra, lifetime measurements, and optical temperature sensing characterization of the $Tb^{3+}/CaMoO_4$ samples were conducted using an optical parametric oscillator (OPO) (Opotek Vibrant 355 LD) pumped by a pulsed Nd^{3+}/YAG laser source. The emission spectra were recorded using a Horiba-Yvon iHR-550 monochromator coupled with an Andor iStar 320T ICCD detector. For temperature-dependent measurements, the samples were subjected to controlled temperature variations from 293 to 333 K using a Lake Shore model 331S temperature controller connected to a type E thermocouple. The fluorescence intensity ratio (FIR) method was applied by monitoring variations in emission intensity at 620 nm under different excitation wavelengths (379 and 544 nm) as a function of temperature.

AUTHOR INFORMATION

Corresponding Author

Luis H. C. Andrade − *Grupo de Espectroscopia Óptica e Fototérmica-GEOF, Centro de Estudos em Recursos Naturais-CERNA, Universidade Estadual de Mato Grosso do Sul-UEMS, Dourados, Mato Grosso do Sul 79804-970, Brazil;* orcid.org/0000-0001-7442-2554;
Email: luishca@uems.br

Authors

Daniela F. Duarte − *Grupo de Espectroscopia Óptica e Fototérmica-GEOF, Centro de Estudos em Recursos Naturais-CERNA, Universidade Estadual de Mato Grosso do Sul-UEMS, Dourados, Mato Grosso do Sul 79804-970, Brazil*

Gilberto J. Arruda − *Grupo de Espectroscopia Óptica e Fototérmica-GEOF, Centro de Estudos em Recursos Naturais-CERNA, Universidade Estadual de Mato Grosso do Sul-UEMS, Dourados, Mato Grosso do Sul 79804-970, Brazil;* orcid.org/0000-0001-8297-3620

Luiz A. O. Nunes − *Instituto de Fisica de São Carlos-IFSC, Universidade de São Paulo-USP, São Carlos, São Paulo 13566-590, Brazil*

Sandro M. Lima − *Grupo de Espectroscopia Óptica e Fototérmica-GEOF, Centro de Estudos em Recursos Naturais-CERNA, Universidade Estadual de Mato Grosso do*

Sul-UEMS, Dourados, Mato Grosso do Sul 79804-970, Brazil; orcid.org/0000-0002-3270-6628

Complete contact information is available at:
https://pubs.acs.org/10.1021/acsaom.5c00208

Funding

The Article Processing Charge for the publication of this research was funded by the Coordenacao de Aperfeicoamento de Pessoal de Nivel Superior (CAPES), Brazil (ROR identifier: 00x0ma614).

Notes

The authors declare no competing financial interest.

ACKNOWLEDGMENTS

The authors thank Coordenação de Aperfeiçoamento de Pessoal de Nível Superior (CAPES), Conselho Nacional de Desenvolvimento Científico e Tecnológico (CNPq), and Fundação de Apoio ao Desenvolvimento do Ensino, Ciência e Tecnologia do Estado de Mato Grosso do Sul (FUNDECT, grant 71/027.247/20224) for financial support.

REFERENCES

(1) Bouzin, M.; Marini, M.; Zeynali, A.; Borzenkov, M.; Sironi, L.; D'Alfonso, L.; Mingozzi, F.; Granucci, F.; Pallavicini, P.; Chirico, G.; Collini, M. Photo-Activated Raster Scanning Thermal Imaging at Sub-Diffraction Resolution. *Nat. Commun.* **2019**, *10* (1), 1−9.

(2) Peng, H.; Stich, M. I. J.; Yu, J.; Sun, L. N.; Fischer, L. H.; Wolfbeis, O. S. Luminescent Europium(III) Nanoparticles for Sensing and Imaging of Temperature in the Physiological Range. *Adv. Mater.* **2010**, *22* (6), 716−719.

(3) Kusama, H.; Sovers, O. J.; Yoshioka, T. Line Shift Method for Phosphor Temperature Measurements This. *Jpn. J. Appl. Phys.* **1976**, *15* (12), 2349−2358.

(4) Morassuti, C. Y.; Nunes, L. A. O.; Lima, S. M.; Andrade, L. H. C. Eu3+- Doped Alumino-Phosphate Glass for Ratiometric Thermometer Based on the Excited State Absorption. *J. Lumin.* **2018**, *193* (September 2017), 39−43.

(5) Marciniak, L.; Waszniewska, K.; Bednarkiewicz, A.; Hreniak, D.; Strek, W. Sensitivity of a Nanocrystalline Luminescent Thermometer in High and Low Excitation Density Regimes. *J. Phys. Chem. C* **2016**, *120* (16), 8877−8882.

(6) Zhao, Y.; Wang, X.; Zhang, Y.; Li, Y.; Yao, X. Optical Temperature Sensing of Up-Conversion Luminescent Materials: Fundamentals and Progress. *J. Alloys Compd.* **2020**, *817*, 152691.

(7) Sleigth, A. W. Accurate Cell Dimensions for ABO4 Molybdates and Tungstates. *Biochim. Biophys. Acta* **1962**, *63*, 2899.

(8) Andrade, L. H. C.; Li, M. S.; Guyot, Y.; Brenier, A.; Boulon, G. Optical Multi-Sites of Nd3+-Doped CaMoO4 Induced by Nb5+ Charge Compensator. *J. Phys.: Condens. Matter* **2006**, *18* (34), 7883−7892.

(9) Nobre, F. X.; Muniz, R.; Martins, F.; Silva, B. O.; de Matos, J. M. E.; da Silva, E. R.; Couceiro, P. R. C.; Brito, W. R.; Leyet, Y. Calcium Molybdate: Toxicity and Genotoxicity Assay in Drosophila Melanogaster by SMART Test. *J. Mol. Struct.* **2020**, *1200*, 127096.

(10) Tranquilin, R. L.; Lovisa, L. X.; Almeida, C. R. R.; Paskocimas, C. A.; Li, M. S.; Oliveira, M. C.; Gracia, L.; Andres, J.; Longo, E.; Motta, F. V.; Bomio, M. R. D. Understanding the White-Emitting CaMoO4 Co-Doped Eu3+, Tb3+, and Tm3+ Phosphor through Experiment and Computation. *J. Phys. Chem. C* **2019**, *123* (30), 18536−18550.

(11) Jung, J. Y. White Luminescent Calcium Molybdate Phosphor Synthesized at Room Temperature via the Co-Precipitation Method Used in a LED Flexible Composite. *Opt. Mater.* **2022**, *132* (June), 112830.

(12) Verma, A.; Sharma, S. K. Dual-Mode Luminescence: A New Perspective in Calcium Molybdate Phosphor for Solar Cell Application. *J. Mater. Sci.: Mater. Electron.* **2019**, *30*, 11778−11789.

(13) Bharat, L. K.; Raju, G. S. R.; Yu, J. S. Red and Green Colors Emitting Spherical-Shaped Calcium Molybdate Nanophosphors for Enhanced Latent Fingerprint Detection. *Sci. Rep.* **2017**, *7* (1), 11571.

(14) Tranquilin, R. L.; Oliveira, M. C.; Santiago, A. A. G.; Lovisa, L. X.; Ribeiro, R. A. P.; Longo, E.; de Lazaro, S. R.; Almeida, C. R. R.; Paskocimas, C. A.; Motta, F. V.; Bomio, M. R. D. Presence of Excited Electronic States on Terbium Incorporation in CaMoO4: Insights from Experimental Synthesis and First-Principles Calculations. *J. Phys. Chem. Solids* **2021**, *149*, 109790.

(15) Bhagwan, J.; Hussain, S. K.; Yu, J. S. Facile Hydrothermal Synthesis and Electrochemical Properties of CaMoO4 Nanoparticles for Aqueous Asymmetric Supercapacitors. *ACS Sustain. Chem. Eng.* **2019**, *7* (14), 12340−12350.

(16) Wang, Y.; Ma, J.; Tao, J.; Zhu, X.; Zhou, J.; Zhao, Z.; Xie, L.; Tian, H. Low Temperature Synthesis of CaMoO4 Nanoparticles. *Ceram. Int.* **2007**, *33* (4), 693−695.

(17) Peng, G. H.; Li, N.; Liang, Z. H.; Wang, X.; Wu, J. L.; Wang, X. F. Hydrothermal Synthesis and Luminescence Properties of 3D Walnut-like CaMoO4:Eu3+ Red Phosphors. *J. Alloys Compd.* **2014**, *599*, 102−107.

(18) Antunes Filho, S.; dos Santos, M. S.; dos Santos, O. A. L.; Backx, B. P.; Soran, M. L.; Opriş, O.; Lung, I.; Stegarescu, A.; Bououdina, M. Biosynthesis of Nanoparticles Using Plant Extracts and Essential Oils. *Molecules* **2023**, *28* (7), 3060.

(19) Li, X.; Yang, Z.; Guan, L.; Guo, J.; Wang, Y.; Guo, Q. Synthesis and Luminescent Properties of CaMoO4:Tb3+, R+ (Li+, Na+, K+). *J. Alloys Compd.* **2009**, *478* (1−2), 684−686.

(20) Shackelford, J. F. *Introduction to Materials Science for Engineers*, 8th ed.; Pearson, 2016.

(21) Santiago, A. A. G.; Macedo, E. M.; Oliveira, F. K. F.; Tranquilin, R. L.; Teodoro, M. D.; Longo, E.; Motta, F. V.; Bomio, M. R. D. Enhanced Photocatalytic Activity of CaMoO4/g-C3N4 Composites Obtained via Sonochemistry Synthesis. *Mater. Res. Bull.* **2022**, *146*, 111621.

(22) Gao, H.; Wang, S.; Wang, Y.; Yang, H.; Wang, F.; Tang, S.; Yi, Z.; Li, D. CaMoO4/CaWO4 Heterojunction Micro/Nanocomposites with Interface Defects for Enhanced Photocatalytic Activity. *Colloids Surf., A* **2022**, *642* (February), 128642.

(23) Parchur, A. K.; Ningthoujam, R. S. Preparation and Structure Refinement of Eu3+ Doped CaMoO 4 Nanoparticles. *Dalton Trans.* **2011**, *40* (29), 7590−7594.

(24) Mickymaray, S. One-Step Synthesis of Silver Nanoparticles Using Saudi Arabian Desert Seasonal Plant Sisymbrium Irio and Antibacterial Activity against Multidrug-Resistant Bacterial Strains. *Biomolecules* **2019**, *9* (11), 662.

(25) Soshnikova, V.; Kim, Y. J.; Singh, P.; Huo, Y.; Markus, J.; Ahn, S.; Castro-Aceituno, V.; Kang, J.; Chokkalingam, M.; Mathiyalagan, R.; Yang, D. C. Cardamom Fruits as a Green Resource for Facile Synthesis of Gold and Silver Nanoparticles and Their Biological Applications. *Artif. Cells, Nanomed., Biotechnol.* **2018**, *46* (1), 108−117.

(26) Karolewicz, M.; Fuks, H.; Tomaszewicz, E. Synthesis and Thermal, Optical and Magnetic Properties of New Mn 2 + - Doped and Eu 3 + -Co-Doped Scheelites. *J. Therm. Anal. Calorim.* **2019**, *138* (3), 2219−2231.

(27) Tangboriboon, N.; Phudkrachang, P.; Mulsow, L. O.; Kunchornsup, W.; Sirivat, A. Removal of Water Extractable Proteins from Concentrated Natural Rubber Latex by Eggshells. *J. Elastomers Plast.* **2013**, *45* (3), 253−269.

(28) Saleh, S. H.; Tripp, C. P. Measurement of Water Concentration in Oils Using CaO Powder and Infrared Spectroscopy. *Talanta* **2021**, *228* (January), 122250.

(29) Laguna, M.; Nuñez, N. O.; Bacerro, A. I.; Ocaña, M. Morphology Control of Uniform CaMoO4 Based Self-Assembled Microarchitectures and Development of White Light Emitting

Phosphors by Ln Doping (Ln = Dy^{3+}, Eu^{3+}). *CrystEngComm* **2017**, *19*, 1590−1600.

(30) Parchur, A. K.; Prasad, A. I.; Ansari, A. A.; Rai, S. B.; Ningthoujam, R. S. Luminescence Properties of Tb 3+-Doped CaMoO 4 Nanoparticles: Annealing Effect, Polar Medium Dispersible, Polymer Film and Core-Shell Formation. *Dalton Trans.* **2012**, *41* (36), 11032−11045.

(31) Kim, B. H.; Kim, W.; Kim, T.; Ko, B. M.; Hong, S. J.; Lee, K.; Kim, J.; Song, S. H.; Lee, S. Hydrogen-Bonding-Mediated Molecular Vibrational Suppression for Enhancing the Fluorescence Quantum Yield Applicable for Visual Phenol Detection. *ACS Appl. Mater. Interfaces* **2021**, *13* (45), 54339−54347.

(32) Messing, G. L.; Zhang, S.-C.; Jayanthi, G. V. Ceramic Powder Synthesis by Spray Pyrolysis. *J. Am. Ceram. Soc.* **1993**, *76*, 2707−2726.

(33) Yin, Y.; Gao, Y.; Sun, Y.; Zhou, B.; Ma, L.; Wu, X.; Zhang, X. Synthesis and Photoluminescent Properties of CaMoO4 Nanostructures at Room Temperature. *Mater. Lett.* **2010**, *64* (5), 602−604.

(34) Zhou, X.; Yang, X.; Xiao, T.; Zhou, K.; Chen, T.; Yan, H.; Wang, Z. Luminescence Properties and Energy Transfer of Host Sensitized CaMoO 4:Tb3+ Green Phosphors. *J. Rare Earths* **2013**, *31* (7), 655−659.

(35) Mahlik, S.; Behrendt, M.; Grinberg, M.; Cavalli, E.; Bettinelli, M. High Pressure Luminescence Spectra of CaMoO4:Ln3+ (Ln = Pr, Tb). *J. Phys.: Condens. Matter* **2013**, *25* (10), 105502.

(36) Dixit, P.; Chauhan, V.; Pandey, P. K.; Pandey, P. C. Improvement in Luminescence of Thermally Stable CaMoO4:Tb3+ Green Phosphor by Bi3+ Ions. *Mater. Chem. Phys.* **2023**, *305* (October 2022), 127913.

(37) Lee, H.-W.; Huh, Y. D. Preparation of Transparent Suspensions of Tunable-Emission CaMoO4:(1−x)Eu^{3+}, (x)Tb^{3+} nanophosphors. *Opt. Mater.* **2021**, *111*, 110594.

(38) Xiong, J.; Meng, Q.; Sun, W. Luminescent Properties and Energy Transfer Mechanism from Tb3+ to Eu3+ in CaMoO4:Tb3+,Eu3+ Phosphors. *J. Rare Earths* **2016**, *34* (3), 251−258.

(39) Zhang, Z. J.; Chen, H. H.; Yang, X. X.; Zhao, J. T. Preparation and Luminescent Properties of Eu3+ and Tb3+ Ions in the Host of CaMoO4. *Mater. Sci. Eng., B* **2007**, *145* (1−3), 34−40.

(40) Cavalli, E.; Boutinaud, P.; Mahiou, R.; Bettinelli, M.; Dorenbos, P. Luminescence Dynamics in Tb3+-Doped CaWO4 and CaMoO4 Crystals. *Inorg. Chem.* **2010**, *49* (11), 4916−4921.

(41) Mondal, S.; Manivasagan, P.; Bharathiraja, S.; Santha Moorthy, M.; Nguyen, V. T.; Kim, H. H.; Nam, S. Y.; Lee, K. D.; Oh, J. Hydroxyapatite Coated Iron Oxide Nanoparticles: A Promising Nanomaterial for Magnetic Hyperthermia Cancer Treatment. *Nanomaterials* **2017**, *7* (12), 426.

(42) Drabik, J.; Kowalski, R.; Marciniak, L. Enhancement of the Sensitivity of Single Band Ratiometric Luminescent Nanothermometers Based on Tb3+ Ions through Activation of the Cross Relaxation Process. *Sci. Rep.* **2020**, *10* (1), 1−11.

(43) Stefanska, J.; Marciniak, L.; Chrunik, M. Sensitivity Enhancement of the Tb3+-Based Single Band Ratiometric Luminescent Thermometry by the Metal-to-Metal Charge Transfer Process. *J. Phys. Chem. C* **2021**, *125* (9), 5226−5232.

(44) Wang, C.; Jin, Y.; Zhang, R.; Yao, Q.; Hu, Y. A Review and Outlook of Ratiometric Optical Thermometer Based on Thermally Coupled Levels and Non-Thermally Coupled Levels. *J. Alloys Compd.* **2022**, *894*, 162494.

(45) Kolesnikov, I. E.; Golyeva, E. V.; Lähderanta, E.; Kurochkin, A. V.; Mikhailov, M. D. Ratiometric Thermal Sensing Based on Eu3+-Doped YVO4 Nanoparticles. *J. Nanopart. Res.* **2016**, *18* (12), 354.

(46) Fang, H.; Wei, X.; Zhou, S.; Li, X.; Chen, Y.; Duan, C. K.; Yin, M. Terbium and Holmium Codoped Yttrium Phosphate as Non-Contact Optical Temperature Sensors. *RSC Adv.* **2017**, *7* (17), 10200−10205.

(47) Chen, D.; Wang, Y.; Yu, Y.; Huang, P.; Weng, F. Quantum Cutting Downconversion by Cooperative Energy Transfer from Ce3+ to Yb3+ in Borate Glasses. *J. Appl. Phys.* **2008**, *104* (11), 1−4.

(48) Vetrone, F.; Naccache, R.; Zamarrón, A.; Juarranz de la Fuente, A.; Sanz-Rodríguez, F.; Martinez Maestro, L.; Martín Rodriguez, E.; Jaque, D.; García Solé, J.; Capobianco, J. A. Temperature Sensing Using Fluorescent Nanothermometers. *ACS Nano* **2010**, *4* (6), 3254−3258.

(49) Bünzli, J. C. G.; Piguet, C. Taking Advantage of Luminescent Lanthanide Ions. *Chem. Soc. Rev.* **2005**, *34* (12), 1048−1077.

(50) Keil, T. H. Shapes of Impurity Absorption Bands in Solids. *Phys. Rev.* **1965**, *140*, A601−A617.

(51) Wang, X.; Liu, Q.; Bu, Y.; Liu, C. S.; Liu, T.; Yan, X. Optical Temperature Sensing of Rare-Earth Ion Doped Phosphors. *RSC Adv.* **2015**, *5* (105), 86219−86236.

(52) Parchur, A. K.; Ningthoujam, R. S. Preparation, Microstructure and Crystal Structure Studies of Li+ Co-Doped YPO4:Eu3+. *RSC Adv.* **2012**, *2* (29), 10854−10858.

(53) Singh, J.; Dutta, T.; Kim, K. H.; Rawat, M.; Samddar, P.; Kumar, P. "Green" Synthesis of Metals and Their Oxide Nanoparticles: Applications for Environmental Remediation. *J. Nanobiotechnol.* **2018**, *16* (1), 1−24.

(54) Rani, N.; Singh, P.; Kumar, S.; Kumar, P.; Bhankar, V.; Kumar, K. Plant-Mediated Synthesis of Nanoparticles and Their Applications: A Review. *Mater. Res. Bull.* **2023**, *163* (March), 112233.

(55) Osman, A. I.; Zhang, Y.; Farghali, M.; Rashwan, A. K.; Eltaweil, A. S.; Abd El-Monaem, E. M.; Mohamed, I. M. A.; Badr, M. M.; Ihara, I.; Rooney, D. W.; Yap, P. S. Synthesis of green nanoparticles for energy, biomedical, environmental, agricultural, and food applications: A review. *Environ. Chem.* **2024**, *22*, 841−887.

(56) Abuzeid, H. M.; Julien, C. M.; Zhu, L.; Hashem, A. M. Green Synthesis of Nanoparticles and Their Energy Storage, Environmental, and Biomedical Applications. *Crystals* **2023**, *13* (11), 1576.

(57) Yu, H.; Shi, X.; Huang, L.; Kang, X.; Pan, D. Solution-Deposited and Low Temperature-Annealed Eu3+/Tb3+-Doped CaMoO4/SrMoO4 Luminescent Thin Films. *J. Lumin.* **2020**, *225* (May), 117371.

(58) Gao, Y.; Huang, F.; Lin, H.; Zhou, J.; Xu, J.; Wang, Y. A Novel Optical Thermometry Strategy Based on Diverse Thermal Response from Two Intervalence Charge Transfer States. *Adv. Funct. Mater.* **2016**, *26* (18), 3139−3145.

(59) Ding, M.; Xu, M.; Chen, D. A New Non-Contact Self-Calibrated Optical Thermometer Based on Ce3+ → Tb3+ → Eu3+ Energy Transfer Process. *J. Alloys Compd.* **2017**, *713*, 236−247.

(60) Zhang, X.; Wu, Z. C.; Mo, F.; Li, N.; Guo, Z.; Zhu, Z. Insight into Temperature-Dependent Photoluminescence of LaOBr: Ce3+, Tb3+ Phosphor as a Ratiometric and Colorimetric Luminescent Thermometer. *Dyes Pigm.* **2017**, *145*, 476−485.

(61) Zhang, Y.; Liu, J.; Zhang, H.; He, Q.; Liang, X.; Xiang, W. Ultra-Stable Tb3+: CsPbI3 Nanocrystal Glasses for Wide-Range High-Sensitivity Optical Temperature Sensing. *J. Eur. Ceram. Soc.* **2020**, *40* (15), 6023−6030.